ORIGINAL ARTICLE

# Study on anti-wear property of 3D printed-tools in friction stir welding by numerical and physical experiments

**Jian Luo · Hong Wang · Wei Chen · Longfei Li**

**Abstract** Friction wear is a key factor influencing the life of friction stir welding (FSW) tools. One of the challenging problems in the field of FSW is improving anti-wear properties and extending the service life of tools. Based on Archard theory, a rigid-plastic mathematical-physical model describing the friction wear behavior of the tool during FSW process was established. The friction wear behavior and surface features of the tool during plunging and welding stage were studied by numerical and physical experiments. The effects of welding parameters and geometrical features of the tool on friction wear behavior were analyzed. 7075 aluminum alloy was chosen as the welding material and the tool was designed and manufactured by 3D printing. These numerical and physical experiments were compared. The results show that the tool fabricated from turning consisted of tempered martensite, while the tool produced from selective laser melting showed layers of banded structure with inhomogeneous directions. The average microhardness of the latter was higher than that of the former. The wear loss of the FSW tool during plunge stage increases with the increasing of the rotation speed and plunge speed. Meanwhile, the wear depth of the tool increases with raising the rotation speed at a constant welding speed. The weight of FSW tool decreases with increasing welding distance. The microstructure of the stir made by the selective laser melting is beneficial to improve the anti-wear property. The manufacturing process method can affect the tool's lifetime seriously with the same material used. The simulation results are shown to be in good agreement with experimental data. The study also provides theoretical and practical guidance for predicting the wear of FSW tools.

## 1 Introduction

The friction stir welding tool is a core study object in friction stir welding (FSW) research. The main effects of the tool are heating and softening the welded material, destroying the oxidation layer on workpiece surface, and driving the plastic material flow [1]. The size and geometry of FSW tools have a great effect on the microstructure and mechanical properties of the joint [2–4], and the design of FSW tools is a key factor to obtain high-quality joint. The tool experiences a combination effect of high temperature, forging pressure, friction torque, and welding resistance during welding. So, long-time working will lead to the failure and shortening of the lifespan of the tool [5–7]. Wear is the most crucial element which affects the FSW tool's life, and it's also one of the main reasons that cause failure. The wear of the FSW tool will seriously reduce welding efficiency, increase production cost, and shorten the tool's lifespan [8]. Due to the huge difference between the hardness of FSW tools and light alloy workpieces like magnesium and aluminum, the wear volume fraction is negligible. Nevertheless, when applied to high strength and hardness material, the wear resistance of the FSW tool is a key factor to decide whether the welding process can last for a long duration, or whether a high-quality joint can be obtained. Therefore, the research of FSW tool wear is of great significance.

Many experiment and simulation researches were conducted on FSW tool wear. Sato Yutaka S. et al. [9] studied the wear of the FSW tool during welding and the microstructural evolution of the weld. W. M. Zeng et al. [10] investigated the effects of different pin wear

J. Luo (✉) · H. Wang · W. Chen · L. Li
State key laboratory of Mechanical Transmission, Chongqing University, Chongqing 400030, People's Republic of China
e-mail: luojian2007@gmail.com

levels on joint quality, and the results showed that the wear led to formation of voids in the stir zone and further resulted in the decrease of tensile strength and yield strength. A. Farias et al. [11] carried out the FSW experiment on titanium utilizing the tool made of cemented carbide. The results of metallographic analysis showed no internal defects in the welds. However, the tool experienced severe wear due to heat adhesive and elements diffusion, causing loss of weld surface and fragments inside the joint. Siddiquee et al. [12] investigated the effect of FSW parameters on the wear and deformation behavior of tungsten carbide (WC) tool with different levels of shoulder diameter, tool rpm, and traverse speed. The results showed that wear at the pin root and bottom face of the pin attributed to diffusion and attrition mechanisms, respectively. FSW of aluminum matrix composite (including strengthening phase likes SiC and $Al_2O_3$) is also a research focus for its spread applications in aerospace industry. T. Prater et al. [13–18] established the wear model and explored influences of the size and mass fraction of strengthening phase on the wear of FSW tool through the change of mass and geometry and observation of surface topography. B. Gibson et al. [19] proposed self-adjusting torque controller, which could predict the pin profile during welding process precisely. Simulation is an effective and cost-saving way to study tool wear. S. Mandal et al. [20–22] simulated the tool wear during the plunging stage, and results showed that the adoption of donor material reduced the wear extent of FSW tool.

It is an effective way to reduce wear through selecting tool material with high hardness, high temperature, and wear resistance properties [23]. In addition, the manufacturing method of FSW tools is another factor to affect wear. Direct metal laser sintering (DMLS) is a new 3D print manufacturing or AM process which can fabricate parts directly by layer-by-layer laser sintering of metal powder according to CAD data [24]. These new way gets rid of reliance on mold tools, and provides the potential for virtually unlimited complexity and design freedom, allowing the manufacture of complex internal structure and free-form geometry [25]. Compared with conventional manufacturing methods, components fabricated by DMLS can not only meet requirements, but also have improvement in their performance in service as quicker production. So far, DMLS also has some problems of poor micro- and macrostructure and residual stress in any materials, and few public literatures studied the wear of the tool made by 3D print manufacturing.

In this paper, a rigid-viscoplastic model based on the Archard wear theory was established to simulate the wear of a FSW tool with three-chute cavity shoulder and three-slope conical thread pin. The influences of process parameters and geometry features on the wear
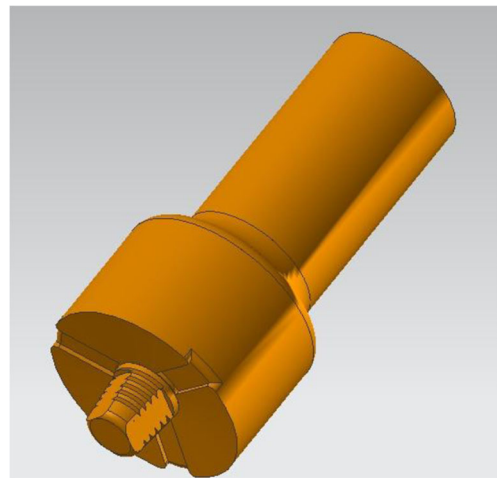


**Fig. 1** Three-dimensional model of the FSW tool

behavior of FSW tool during the plunge stage and welding stage were studied. A FSW experiment was conducted on 7075 aluminum workpiece using a 3D print-manufactured FSW tool, and the experiment data was compared with the simulation result. The numerical results were in good agreement with the experimental results. Those data provide theoretical and practical evidence for researches on FSW tools, and this is the first study of the effect of the manufacturing process of the same material on friction stir tool's life.

## 2 Numerical model

In this paper, DEFORM-3D software was chosen to simulate FSW for its point tracking function and capability of accurate modeling of processes with severe plastic deformation. And the following assumptions were made: (1) the friction factor between the workpiece and the tool was constant, (2) all of the free surfaces of the workpiece and the tool were exposed to atmosphere under the ambient temperature except the backplate, and (3) the workpiece was fixed in all directions at the lower surface.
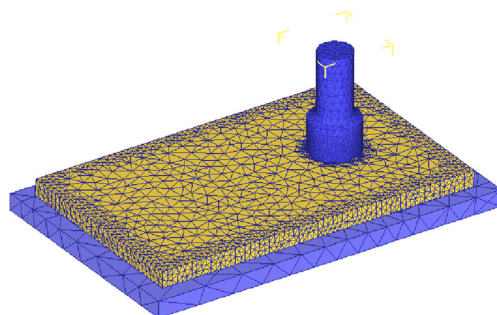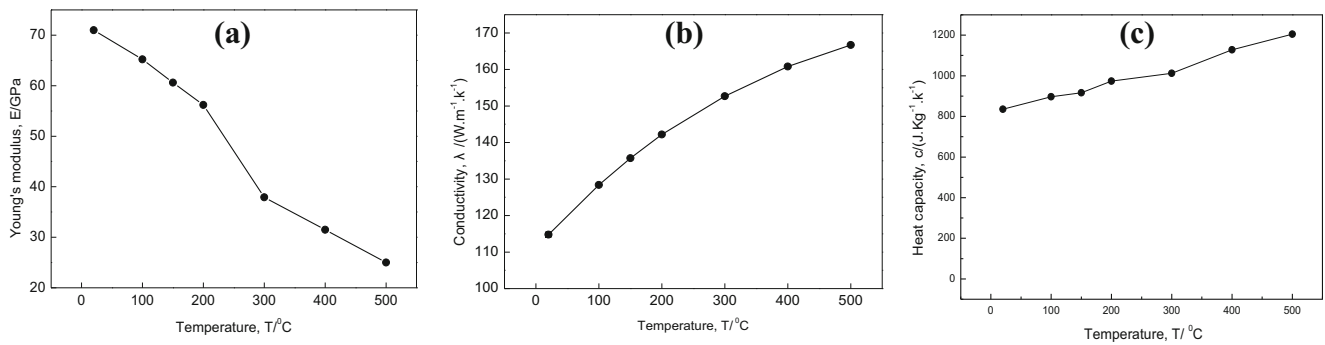


**Fig. 2** Numerical and meshing model

**Fig. 3** The temperature-dependent curves of 7075 aluminum. **a** Young's modulus. **b** Thermal conduction coefficient. **c** Specific heat capacity [31]

## 2.1 Wear model

In FSW process, many factors, such as the rotation speed, the welding speed, and the hardness of welded material, have an effect on the tool wear. Equation 1 in Archard wear theory is suitable for predicting abrasive wear quantitatively, and it can calculate the wear rate of every node of the tool in contact with the workpiece [26–28]. The main advantage of this model is its ability to describe wear behavior based on contact mechanism, and to calculate local wear. According to Eq. 1, the volume of the material removed from the tool due to wear is proportional to the work done by friction forces [29]. The effect of temperature variation on the hardness of tool was not taken into account and velocity and pressure distribution might have a greater influence on wear profile than hardness [30].

$$W = \int K \times \frac{P^a \cdot v^b}{H^c} dt \qquad (1)$$

where $W$ represents wear volume, $P$ is contact pressure between the FSW tool and the workpiece, $v$ is the relative sliding velocity, $H$ is the hardness of the tool, and $dt$ is the time increment. The experimentally calibrated coefficients $a$, $b$, and $c$, were equal to 1, 1, and 2, respectively, in this paper. $K$ is a measurement of the wear intensity which can be obtained by repeated experiment. $K$ is $2e-6$ when the tool material is H13 steel.

## 2.2 Finite element model

The three-dimensional model of the tool with three-chute cavity shoulder and three-slope conical thread pin was established using UG7.5 software, as shown in Fig. 1. Then, it was imported into DEFORM software to establish the finite element model of FSW shown in Fig. 2 after the file format were converted to STL.

Tetrahedron elements were adopted to mesh tool and workpiece for the purpose of simulating material deformation during the FSW process. The tool and the workpiece were defined as rigid and plastic objects initially meshed with 19,537 and 21,131 elements. In order to improve the accuracy and efficiency of the simulation, local re-meshing technique on the basis of former FEM was used for the observation of geometry features of the tool. When the variation of elements near the tool tip was larger than 70 %, the automatic re-meshing function would be triggered. Both the material of the tool and the backplate were H13 steel and the workpiece material was defined as 7075 aluminum with a dimension of 100 mm in width, 60 mm in length, and 5 mm in height. The axial amount of indentation was 0.1 mm. The hardness of the tool was set to a constant of 45 HRC in order to simplify the model.
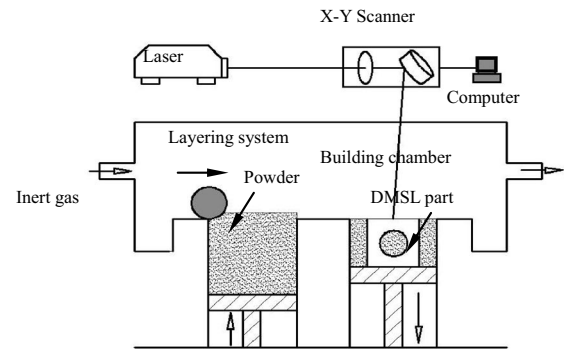
## 2.3 Material models

An appropriate material model that conforms to practical scenarios is of great significance for obtaining accurate simulation results. Young's modulus, heat conduction co-efficient, and capacity for 7075 aluminum varying with temperature are described in Fig. 3a–c, respectively. The thermal characteristics and physical properties of H13

**Table 1** Mechanical and physical properties of H13 steel [32]

| Name | Value |
| --- | --- |
| Material | H13 tool steel |
| Density | 7800 kg/m$^3$ |
| Young's modulus | 211 GPa |
| Poisson ratio | 0.3 |
| Thermal expansion coefficient | 1.242e-5 mm/K |
| Thermal conduction coefficient | 284 W/(m·K) |
| Specific heat capacity | 560 J/(kg·K) |
| Hardness | 363 HV |

**Fig. 4** The DMSL equipment of EOSINT M280 and the manufacturing schematic diagram

steel were assumed to be constant, as shown in Table 1. Under the condition of high strain rate deformation, high precision flow stress models are highly necessary to represent work material constitutive behavior. The work material model represents plastic, elastic, and thermal-mechanical behavior of the material deformation during FSW process. Strain, strain rate, and temperature effects were determined, respectively, by Eq. 2.

$$\overline{\sigma} = \left[ A + B\left(\overline{\varepsilon}\right)^n \right] \left[ 1 + CIn\left(\frac{\dot{\overline{\varepsilon}}}{\dot{\overline{\varepsilon}}_0}\right) \right] \left[ 1 - \left(\frac{T - T_o}{T_m - T_0}\right)^m \right] \quad (2)$$

In the Johnson-Cook model, $\sigma$ is effective stress; the constant $A$ represents the initial yield strength of the material at room temperature; $B$, $C$, and $m$ are constants; and strain rate $\dot{\overline{\varepsilon}}$ is the plastic equivalent strain which is normalized with a reference strain rate. $T_m$ is the melting temperature, $n$ is the work hardening exponent, and $T_0$ is the ambient temperature. In the present study, the values of $A$, $B$, and $C$ were set to be 369 MPa, 684 MPa, and 0.0083, respectively [21].

### 2.4 Boundary conditions

The movements of lower surface of 7075 aluminum in all directions were limited. In the initial stage, the temperature of the workpiece and the tool was equal to ambient temperature. The shear model (Eq. 3) was used to describe contact situation between the tool and the workpiece.

$$f = mk \quad (3)$$

where $f$ denotes the frictional stress, $k$ is the shear yield stress, and $m$ represents the friction factor which was set to 0.4 in this paper. Heat transfer coefficient between the workpiece and the

backplate/tool is 22,000 W/(m²·°C), and the convection coefficient between the workpiece and air is 20 W/(m²·°C).
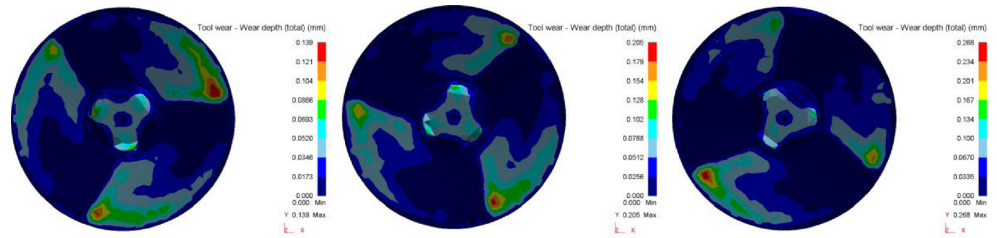
## 3 Experiments

The FSW tool was made from EOS tool steel powder by the EOSINT M 280 machine (Fig. 4). The technical data of EOSINT M 280 is shown in Table 2. Then, it was stress relieved at 790 °C for 90 min and cooled naturally in the furnace before being removed from the
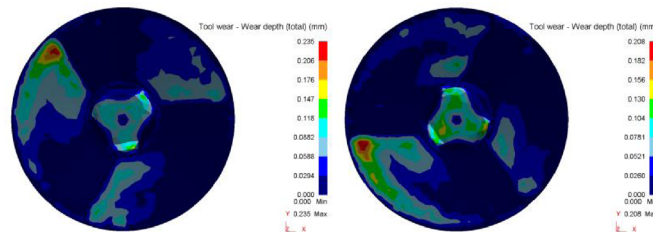
**Table 2** Technical data of EOSINT M280

| | |
|---|---|
| Building volume (including building platform) | 250 mm×250 mm×325 mm (9.85×9.85×12.8 in.) |
| Laser type | Yb-fiber laser, 200 or 400 W (optional) |
| Precision optics | F-theta-lens, high-speed scanner |
| Scan speed | Up to 7.0 m/s (23 ft./s) |
| Variable focus diameter | 100–500 μm (0.004–0.02 in.) |
| Power supply | 32 A |
| Power consumption | Maximum 8.5 kW/typical 3.2 kW |
| Nitrogen generator | Integrated |
| Compressed air supply | 7000 hPa; 20 m³/h (102 psi; 706 ft³/h) |
| Dimensions (W×D×H) | |
| System | 2200 mm×1070 mm×2290 mm (86.6×42.1×90.1 in.) |
| Recommended installation space | Min. 4.8 m×3.6 m×2.9 m (189×142×114 in.) |
| Weight | Approx. 1250 kg (2756 lb) |
| Data preparation | |
| Software | EOS RP Tools; EOSTATE Magics RP (materialize) |
| CAD interface | STL. optional: converter for all standard formats |
| Network | Ethernet |

**Fig. 5** The wear contour of FSW tool at plunge stage under different parameters. **a** $\omega$=600r/min, $v_x$=1.2mm/s. **b** $\omega$=800r/min, $v_x$=1.2mm/s. **c** $\omega$=1000r/min, $v_x$=1.2mm/s. **d** $\omega$=1000r/min, $v_x$=1.0mm/s. **e** $\omega$=1000r/min, $v_x$=0.8mm/s

**(a)** $\omega = 600r/\min, v_x = 1.2mm/s$; **(b)** $\omega = 800r/\min, v_x = 1.2mm/s$; **(c)**

$\omega = 1000r/\min, v_x = 1.2mm/s$

**(d)** $\omega = 1000r/\min, v_x = 1.0mm/s$; **(e)** $\omega = 1000r/\min, v_x = 0.8mm/s$

titanium base plate by wire electrical discharge machining. The mass of the tool before carrying out the FSW of 7075 aluminum was 28.0 g. The plastic aluminum adhering to the tool surface was removed before analysis by immersing the tool into the sodium hydroxide solution (100 ml H$_2$O+10 g NaOH) for 4 h to etch the aluminum. The wear volume fraction of the tool can be quantitatively calculated by measuring the mass change before and after welding according to Eq. 4. Where $m$ is the initial mass, and $\Delta m$ is the mass loss.
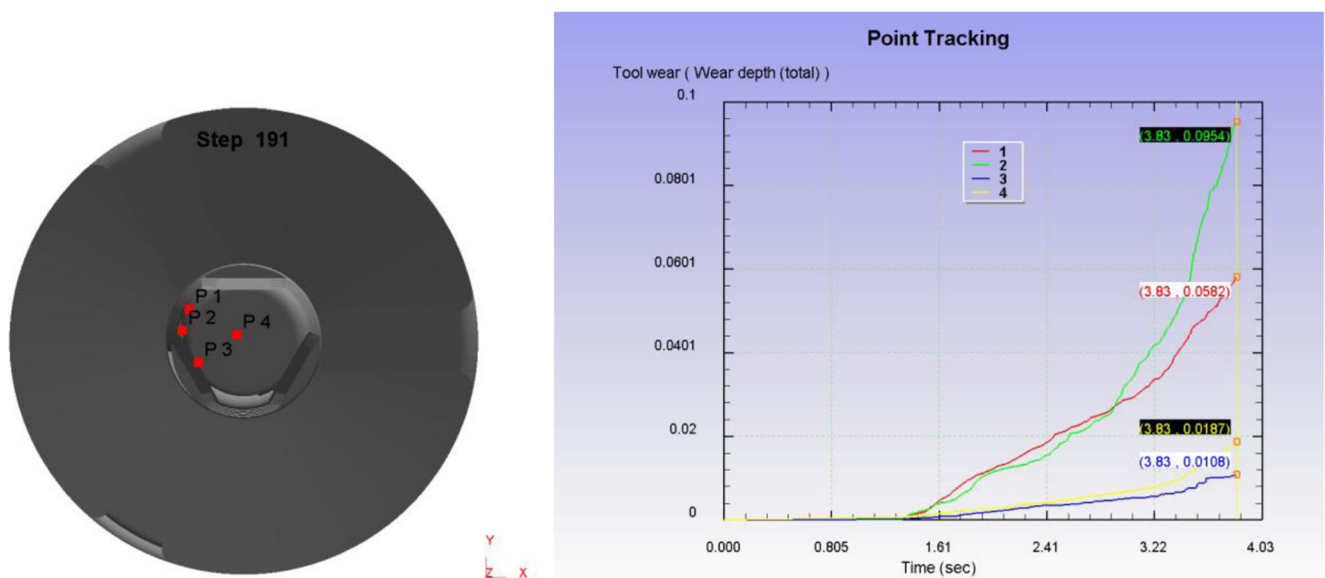
$$\frac{m_i - \Delta m}{m_i} \times 100\% \tag{4}$$

**Fig. 6** The locations of end face tracking points and their time-wear curves under $\omega$=600r/min, $v_x$=1.2mm/s
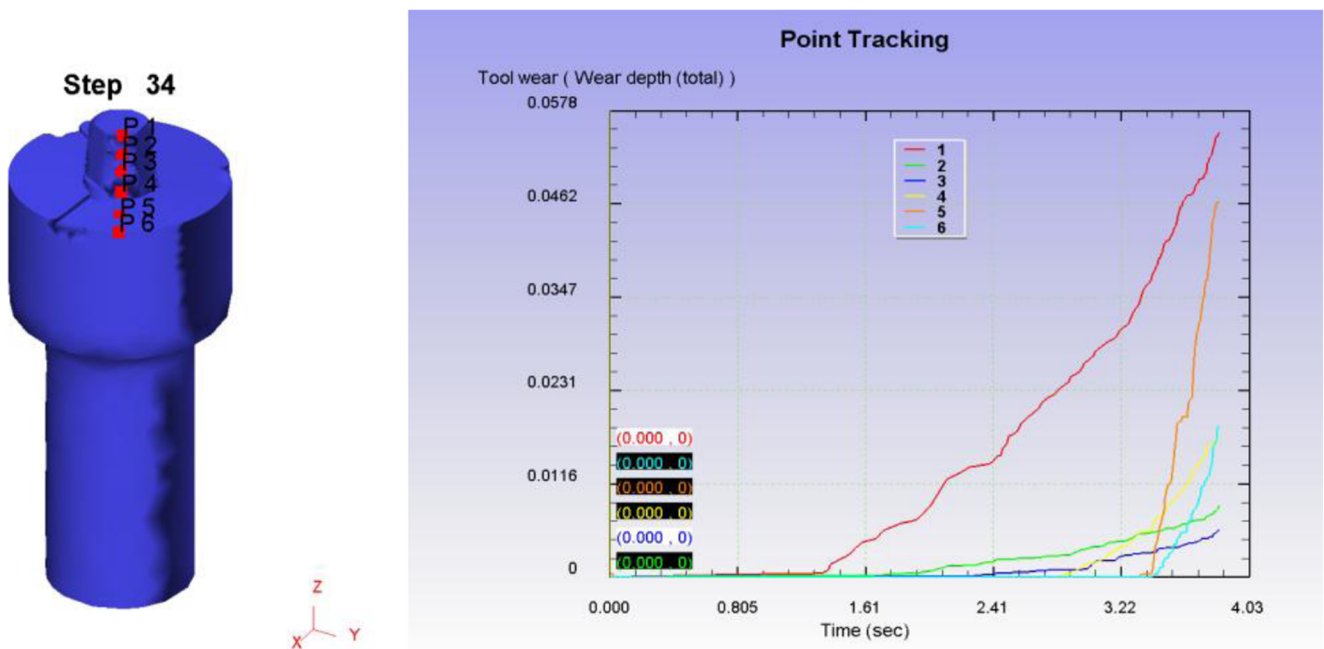
**Fig. 7** The locations of side face tracking points and their time-wear curves under $\omega=600r$/min, $v_x=1.2$mm/s
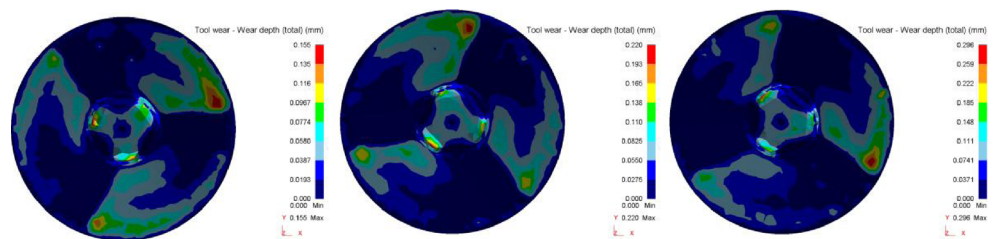
## 4 Results and discussion

### 4.1 Plunging stage

During the plunge stage, the tool was subject to large and non-uniform force, and was prone to wear or even fail [16]. Thus, there is a notable significance to investigate the influence of process parameters on wear behavior of the FSW tool at the plunge stage. Figure 5 shows the wear contour of the FSW tool under different parameters. It can be seen that under a constant plunge speed, tool wear increased by 93.5 % (from 0.139 to

**Fig. 8** The wear contour of FSW tool at welding stage under different parameters. **a** $\omega=600r$/min, $v_m=0.5$mm/s. **b** $\omega=800r$/min, $v_m=0.5$mm/s



**(a)** $\omega = 600r / \min, v_m = 0.5mm / s$ ;**(b)** $\omega = 800r / \min, v_m = 0.5mm / s$ ; **(c)**

$\omega = 1000r / \min, v_m = 0.5mm / s$
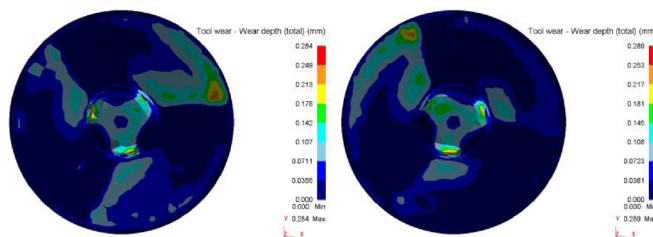


**(d)** $\omega = 1000r / \min, v_m = 0.4mm / s$ ; **(e)** $\omega = 1000r / \min, v_m = 0.6mm / s$
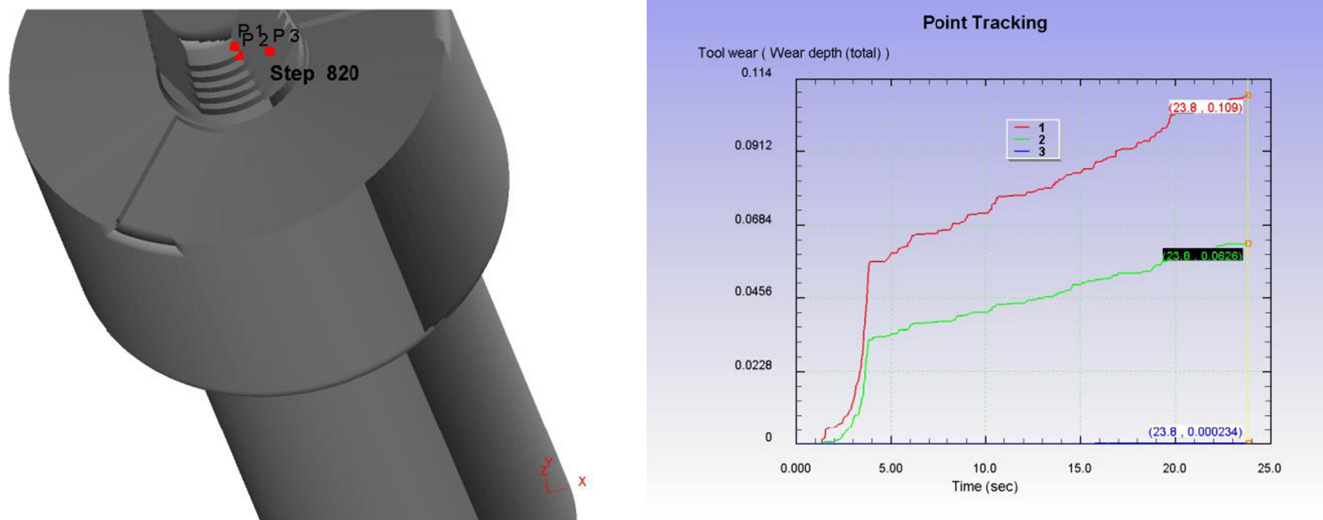
**Fig. 9** The locations of tracking points and their time-wear curves under $\omega = 600 r/\text{min}$, $v_x = 0.5\,\text{mm/s}$

0.268 mm) as the rotational speed increased from 600 to 1000 r/min. Under a constant rotational speed of 1000 r/min, heat input per unit time increased as the plunge speed decreased, which led to the decrease of the fluid pressure of the material and the friction resistance of the tool. Hence, the total wear depth decreased from 0.268 to 0.208 mm.

At the three flumes on the tool shoulder, the wear was slight due to the low contact pressure between the tool and the workpiece. The wear depth was larger at the location closer to the edge of the shoulder, as a result of the larger relative wear velocity. The wear depth distribution was similar under different sets of process parameters.

The point tracing method was applied to study the pin's end-face wear distribution. Figure 6 shows the time-wear curves of the feature points during the wear process. The farther from the geometric center of the end-face, the higher wear can be detected. The maximum wear, which was 0.0954 mm, located at the interface between the inclined plane and the taper surface. The geometric center of the end-face has the minimum wear (0.0108 mm) in virtue of the low relative velocity between the pin and the welded material.

The time-wear curves of the six points radially distributed on the tool shoulder are shown in Fig. 7. Due to the difference of the relative sliding velocity and the contact pressure between the outer and inner diameter of the taper thread during

**Fig. 10** The end-face of the tool. **a** Before welding. **b** After a welding distance of 0.2 m. **c** After a welding distance of 0.4 m. **d** After a welding distance of 0.7 m. **e** After a welding distance of 1.2 m
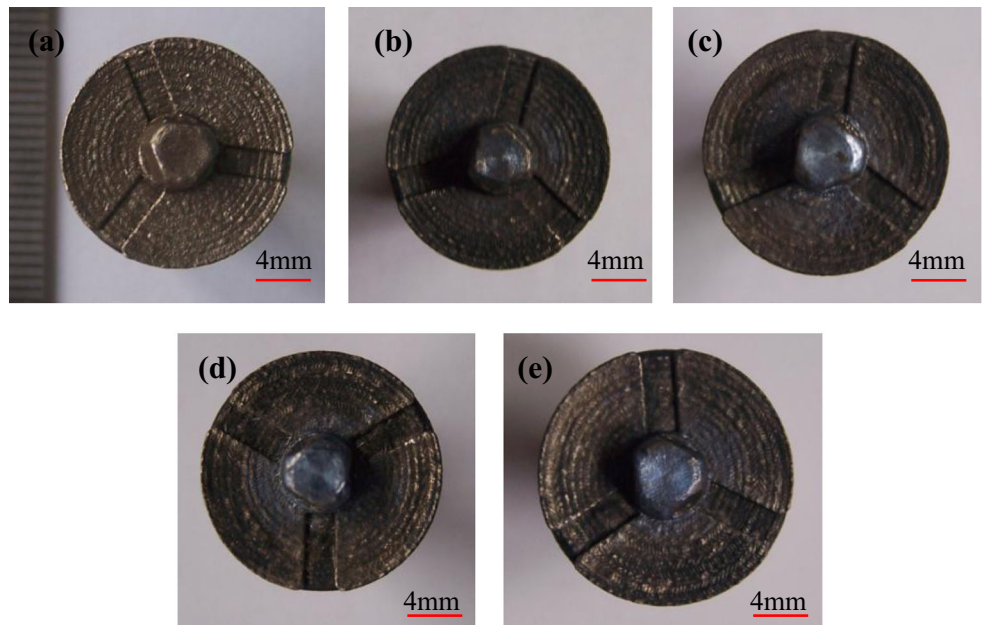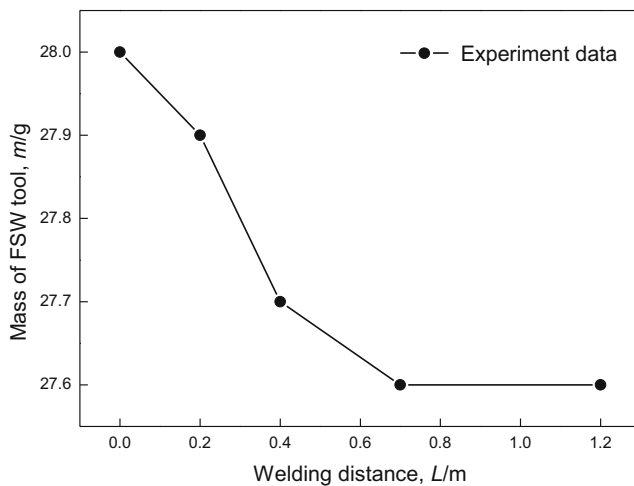
**Fig. 11** The distance-dependent curve of the FSW tool mass

the plunge process, the wear of points on the inner diameter was lower than that on the outer diameter.

### 4.2 Welding stage

Figure 8 shows the wear contour of the tool after welding for 10 mm under different rotational speed and welding speed. It can be seen that under a constant welding speed of 0.5 mm/s, the wear depth of the tool increased from 0.155 to 0.296 mm as the rotational speed increased; whereas under a constant rotational speed of 1000 r/min, the wear depth of the tool changed slightly. The wear depth was 0.284, 0.296, and 0.289 mm, respectively, with the welding speed of 0.4, 0.5, and 0.6 mm/s.

The degree of wear will change with factors such as temperature, contact pressure, and the material flow velocity near the geometric features of the tool surface.
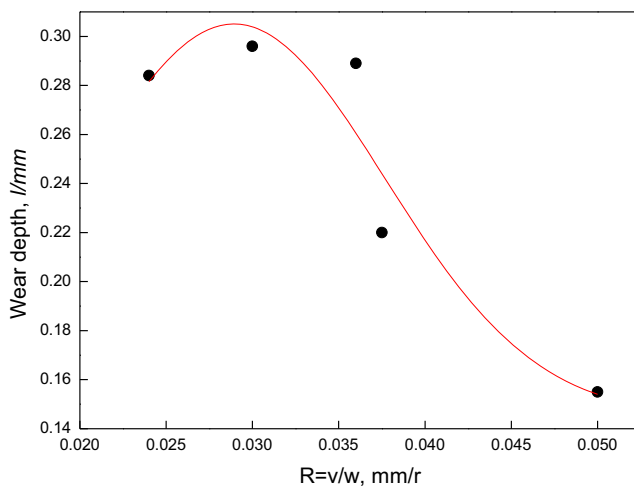


**Fig. 12** The variant curve on welding/rotation ratio and maximum wear depth

Figure 9 shows the wear depth of three feature points on the pin surface during the entire welding stage. It can be seen that point 2, which is located in the groove of the thread, showed almost no wear owing to the low contact pressure during welding. Point 1 at the interface between the inclined plane and the taper surface and point 3 on the inclined plane experienced severe wear during the plunge stage. At the welding stage, the wear depth at points 2 and 3 increased gradually with the increase of the welding distance. And since the plastic material at point 1 had a relatively higher flow velocity, its wear depth was larger than that at point 3.

### 4.3 Experimental verification

The validation experiment for numerical simulation used 7075 aluminum alloy as workpiece under the rotational speed of 1000 r/min and welding speed of 0.5 mm/min. Figure 10 shows the end-face of the tool before and after welding, and from (b) to (e) the length of the weld ranged from 0.2 to 1.2 m. As can be seen from the figure, due to the continuous effect of friction heat during the welding process, the end surface turned black. In addition, the wear of the end-face became more severe with the increase of the welding distance.

Figure 11 indicates the relationship between the mass of the tool and welding distance. When the welding distance increased from 0.2 to 1.2 m, the tool mass loss caused by wear gradually reduced at the initial stage of welding, and then remained constant. However, due to the large differences between the physical properties of the tool steel and the workpiece material, mass loss caused by wear was small. With a welding distance of 1.2 m, the mass loss was only 1.07 %.

### 4.4 Relationship between ratio R and wear volume fraction

According to Archard wear theory model, the wear of the tool is related to both relative sliding speed and contact pressure between tool surface and workpiece. The ratio of welding speed to rotation speed, $R$, represents the heat input during welding process. The $R$-dependent tool mass loss curve derived from experimental data is shown in Fig. 12. The proposed fitting formula is shown in Eq. (5), where $W$ is the maximum wear depth and $R$ is the ratio of welding speed to rotation speed.

$$W = 0.14529 + 0.251e^{-2\frac{(R-0.02893)^2}{0.0003}} \tag{5}$$

The maximum wear depth of the tool increased with the increase of $R$ based on the fitting curve and the formula, and
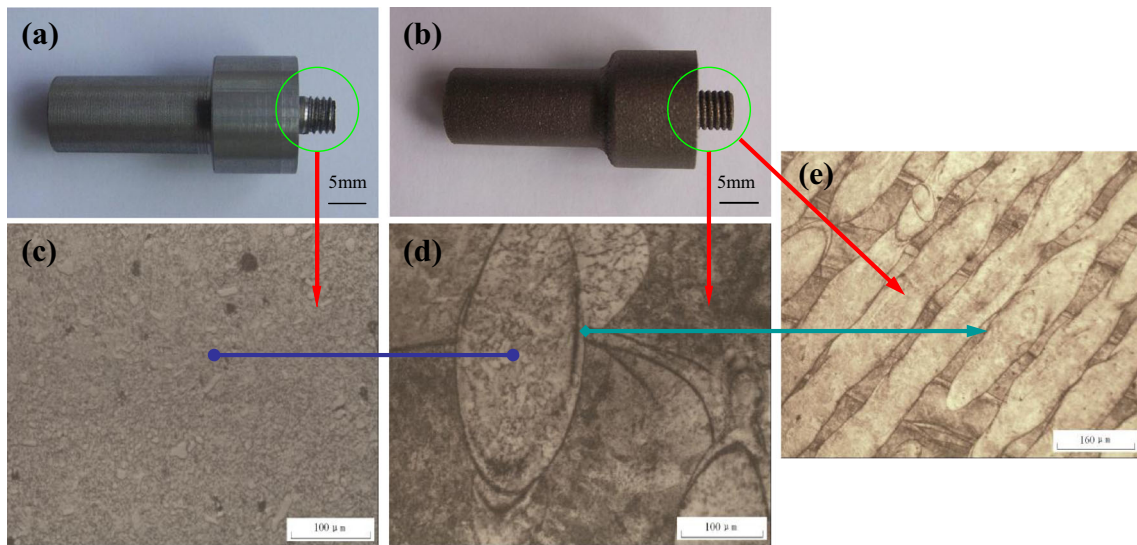
**Fig. 13** Macrostructure and microstructure of tools. **a** Macrostructure of traditional turning stir. **b** Macrostructure of selective laser melting stir. **c** Microstructure of traditional turning stir. **d, e** Microstructure of selective laser melting stir

reached its maximum value when $R$ was 0.02893. Then, the wear depth stayed stable by continuously increasing $R$.

### 4.5 Discussion

Figure 13 shows the difference of the H13 steel stir's macrostructure and microstructure between two fabricated methods: (1) traditional turning and (2) selective laser melting. The tool fabricated by turning consisted of tempered martensite (Fig. 13c), while the tool produced from selective laser melting showed layers of banded structure with inhomogeneous directions (Fig. 13e). The microstructure inside the bands, as shown in Fig. 13d, was similar to that of the tool fabricated by turning. The banded structure in the 3D-printed tool was formed after the solidification of the melted metal powder. Each band had a boundary—solidification boundary. These boundaries could serve as obstacles to grain boundary sliding and thus could increase the resistance to deformation and wear. As

illustrated in Fig. 14, under certain force, grains without a solidification boundary might experience grain boundary sliding, which would result in plastic deformation. This is how tool wear would take place. However, grains with a solidification boundary would possess higher stiffness. Therefore, those materials, although under the same force, are more likely to experience elastic deformation rather than plastic deformation because of the constraint provided by solidification boundaries. Thus, tools fabricated by selective laser melting have higher wear resistance.

Figure 15 shows the microhardness of tools fabricated by traditional turning and selective laser melting method. There was no obvious variation of microhardness from the center to the edge of both stir tools. For the tool fabricated by selective laser melting, the average microhardness (362.8 HV) was approximately 50 % higher than that by traditional turning (242.2 HV). This result also substantiated the effect of solidification boundary in the 3D-printed tool. The microstructural observation and microhardness



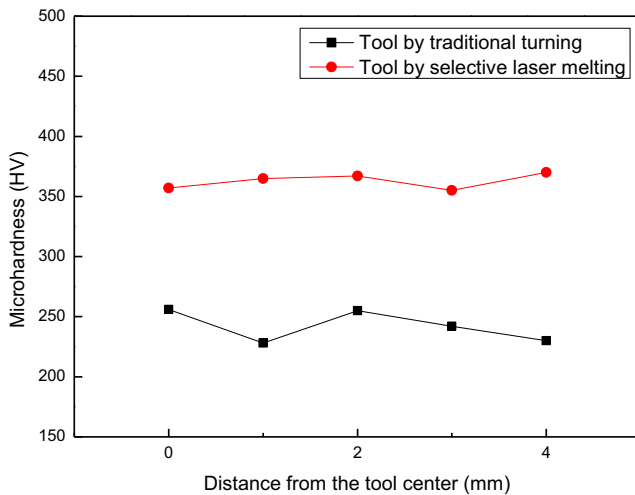**Fig. 14** The effect of solidification boundary on wear deformation
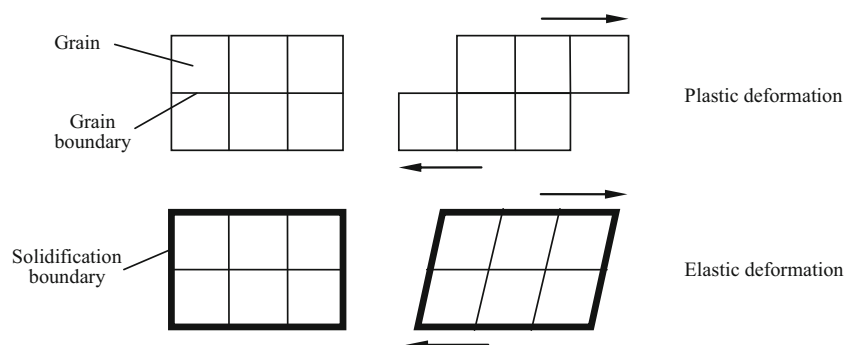
**Fig. 15** Microhardness of tools fabricated by traditional turning and selective laser melting

test together indicated that tools fabricated by selective laser melting would gain higher wear resistance than tools fabricated by turning.

## 5 Conclusions

(1) Under constant plunge speed, the wear depth of the tool was positively related with the speed. With constant rotational speed, the wear depth was negatively related with the plunge speed. The maximum wear depth of the tool end-face occurred at the boundary of the three-chute face and three-slope face.

(2) Since the relative sliding velocity of the tool end-face showed a radially increasing trend, the farther from the geometric center of the tool end-face, the greater tool wear would be produced. On the thread, the wear situation of points on the external diameter of thread was more severe than that on the inner diameter of thread.

(3) The increase of the rotational speed caused an increase in wear depth under constant welding speed. When the rotational speed was 1000 r/min, the maximum wear depth of 0.293 mm occurred at the welding speed of 0.5 mm/s.

(4) As the welding distance increased, the tool mass gradually decreased, but due to the large differences in physical properties between the friction tool and the workpiece, the tool wear remained small. When the welding distance was 0.4 m, the mass loss was 1.07 %. The numerical results of the wear on the tool end-face agreed well with the experiment results.

(5) The solidification boundary in the 3D-printed tool served as obstacles to grain boundary sliding and thus could increase the resistance to plastic deformation and wear. The higher average microhardness of the 3D-printed tool also indicated its higher wear resistance and the effect of solidification boundaries on hindering plastic deformation.

## References

1. Rai R, De A, Bhadeshia HKDH, Debroy T (2011) Review: friction stir welding tools. Sci Technol Weld Join 16:325–342
2. Kumar K, Satish VK (2008) The role of friction stir welding tool on material flow and weld formation. Mater Sci Eng A 485:367–374
3. Tutunchilar S, Haghpanahi M, Bseharatigivi MK, Asadi P, Bahemmat P (2012) Simulation of material flow in friction stir processing of a cast Al-Si alloy. Mater Des 10:415–426
4. Chowdhury SM, Chen DL, Bhole SD, Cao X (2010) Tensile properties of a friction stir welded magnesium alloy: effect of pin tool thread orientation and weld pitch. Mater Sci Eng A 527:6064–6075
5. Mehta M, Arora A, De A, Debroy T (2011) Tool geometry for friction stir welding-optimum shoulder diameter. Metall Mater Trans A 42A:2716–2722
6. Venkatesearlu D, Mandal NR, Mahapatra MM, Harsh SP (2013) Tool design effects for FSW of AA7039. Weld J 92:41s–47s
7. Buffa G, Campanella D, Fratini L (2012) On tool stirring action in friction stir welding of work hardenable aluminum alloys. Sci Technol Weld Join 18:161–168
8. Sato YS, Muraguchi M, Kokawa H (2011) Tool wear and reactions in 304 stainless steel during friction stir welding. Mater Sci Forum 675–677:731–734
9. Park SHC, Yutaka SS, Hiroyuki K, Kazutaka O, Satoshi H, Masahisa I (2009) Boride formation induced by PCBN tool wear in friction-stir-welded stainless steels. Metall Mater Trans A 40A:625–636
10. Zeng WM, Wu HL, Zhang J (2006) Effect of tool wear on micro-structure, mechanical properties and acoustic emission of friction stir welded 6061 Al alloy. Acta Metall Sin 19:9–19
11. Farias A, Batalha GF, Prados EF, Magnabosco R, Delijaicov S (2013) Tool wear evaluations in friction stir processing of commercial titanium Ti–6Al–4V. Wear 302:1327–1333
12. Siddiquee AN, Pandey S (2014) Experimental investigation on deformation and wear of WC tool during friction stir welding (FSW) of stainless steel. Int J Adv Manuf Technol 73:479–486
13. Prater T, Strauss AM, Cook GE, Machemehl C, Sutton P, Cox CD (2010) Statistical modeling and prediction of wear in friction stir welding of a metal matrix composite (Al359/SiC/20P). J Manuf Technol Res 2:1–13
14. Prater TJ, Strauss AM, Cook GE, Gibson BT, Cox CD (2013) A phenomenological model for tool wear in friction stir welding of metal matrix composites. Metall Mater Trans A 44:3757–3764
15. Liu HJ, Feng JC, Fujii H, Nogi K (2005) Wear characteristics of a WC–Co tool in friction stir welding of AC4A + 30 vol%SiCp composite. Int J Mach Tools Manuf 45:1635–1639
16. Prado RA, Murr LE, Shindo DJ, Soto KF (2001) Tool wear in the friction-stir welding of aluminum alloy 6061+20 % Al$_2$O$_3$: a preliminary study. Scripta Mater 45:75–80
17. Prater T, Strauss A, Cook G, Gibson B, Cox C (2013) A comparative evaluation of the wear resistance of various tool materials in friction stir welding of metal matrix composites. J Mater Eng Perform 22:1807–1813
18. Prater T (2014) Friction stir welding of metal matrix composites for use in aerospace structures. Acta Astronaut 93:366–373
19. Gibson B, Cook G, Prater T, Longhurst W, Strauss AM, Cox CD (2013) Adaptive torque control of friction stir welding for the purpose of estimating tool wear. P I Mech Eng B-J Eng 225:1293–1303
20. Mandal S, Rice J, Hou G, Williamson KM, Elmustafa AA (2013) Modeling and simulation of a donor material concept to reduce tool wear in friction stir welding of high-strength materials. J Mater Eng Perform 6:1558–1564

21. Mandal S, Rice J, Elmustafa AA (2008) Experimental and numerical investigation of the plunge stage in friction stir welding. J Mater Process Technol 23:411–419

22. Hamilton R, Mac KD, Li HJ (2010) Multi-physics simulation of friction stir welding process. Eng Comput 27:967–985

23. Shen XJ, Cao L, Li RY (2010) Numerical simulation of sliding wear based on Archard model. 2010 Int Conf Mech Autom Control Eng, pp 325–329

24. Cooper DE, Stanford M, Kibble KA, Gibbons GJ (2012) Additive manufacturing for product improvement at red bull technology. Mater Des 41:226–230

25. Delgado J, Ciurana J, Rodríguez CA (2012) Influence of process parameters on part quality and mechanical properties for DMLS and SLM with iron-based materials. Int J Adv Manuf Technol 60:601–610

26. Hu HJ, Huang WJ (2013) Studies on wears of ultrafine-grained ceramic tool and common ceramic tool during hard turning using Archard wear model. Int J Adv Manuf Technol 69:31–39

27. Rezaei A, Paepegem WV, Baets PD, Ost W, Degrieck J (2013) Adaptive finite element simulation of wear evolution in radial sliding bearings. Wear 296:660–671

28. Groche P, Moeller N, Hoffmann H, Suh J (2011) Influence of gliding speed and contact pressure on the wear of forming tools. Wear 271: 2570–2578

29. Andersson J, Almqvist A, Larsson R (2011) Numerical simulation of a wear experiment. Wear 271:2947–2952

30. Ivan A, Wilson T (2012) Asymptotic modeling of reciprocating sliding wear comparison with finite-element simulations. Eur J Mech A/Solid 34:1–11

31. Ke YL, Dong HY (2004) Pre-stretching process and its application in reducing residual stress of quenched 7075 aluminum alloy thick-plates. China J Nonferrous Metal 14:639–645

32. Yan H, Huab J, Shivpuri R (2005) Numerical simulation of finish hard turning for AISI H13 die steel. Sci Technol Adv Mater 6:540–547